PROCEEDINGS OF SPIE

SPIEDigitalLibrary.org/conference-proceedings-of-spie

Condition assessment of corroded steel rebar in free space using synthetic aperture radar images

Christopher M. Ingemi, Jones Owusu Twumasi, Swinderjit Litt, Tzuyang Yu

Christopher M. Ingemi, Jones Owusu Twumasi, Swinderjit Litt, Tzuyang Yu, "Condition assessment of corroded steel rebar in free space using synthetic aperture radar images," Proc. SPIE 10169, Nondestructive Characterization and Monitoring of Advanced Materials, Aerospace, and Civil Infrastructure 2017, 101691F (19 April 2017); doi: 10.1117/12.2258658

SPIE.

Event: SPIE Smart Structures and Materials + Nondestructive Evaluation and Health Monitoring, 2017, Portland, Oregon, United States

Downloaded From: https://www.spiedigitallibrary.org/conference-proceedings-of-spie on 8/8/2018 Terms of Use: https://www.spiedigitallibrary.org/terms-of-use

Condition Assessment of Corroded Steel Rebar in Free Space using Synthetic Aperture Radar Images

Christopher M. Ingemi, Jones Owusu Twumasi, Swinderjit Litt, Tzuyang Yu
Department of Civil and Environmental Engineering
University of Massachusetts Lowell
One University Avenue, Lowell, MA 01854, U.S.A.

ABSTRACT

Synthetic aperture radar (SAR) imaging of construction materials offers civil engineers an opportunity to better assess the condition of aging civil infrastructures such as reinforced concrete (RC) structures. Corrosion of steel rebar in RC structures is a major problem responsible for their premature failure and unexpected collapse. In this paper, SAR imaging is applied to the quantitative assessment of corroded steel rebar in free space as the first step toward the use of SAR imaging for subsurface sensing of aging RC structures. A 10 GHz stripmap SAR system was used inside an anechoic chamber. The bandwidth of the radar system was 1.5 GHz. Steel rebar specimens were artificially corroded to different levels by regularly applying a mist of 5% NaCl solution for different durations of time in order to simulate the condition of natural corrosion. Two sizes (No. 3 and No. 4) of steel rebar were used in this research. Different orientations of steel rebar were considered. Corrosion level was determined by measuring the mass loss of corroded steel rebar specimens. From our results, feasibility of SAR images for the condition assessment of corroded steel rebar was experimentally demonstrated. It was found that the presence of surface rust on corroded steel rebar reduces the amplitude in SAR images. The SAR image of corroded steel rebar also exhibited a distribution of SAR amplitudes different from the one of intact steel rebar. In addition, it was also found that there is an optimal range for the condition assessment of corroded steel rebar in free space. In our experiment, the optimal range was determined to be 30.4 cm.

Keywords: Synthetic aperture radar imaging, steel rebar corrosion, RC structures, natural corrosion

1. INTRODUCTION

Much of the civil infrastructure in the United States is deteriorating, putting the safety of the citizens of this country at risk and potentially costing the U.S. government billions of dollars in repairs. According to the 2013 Report Card for America's Infrastructure assembled by the American Society of Civil Engineers (ASCE), in America's largest metropolitan areas, structurally deficient bridges are crossed over two hundred million times a day.[1] Traditional inspection methods are inadaquate for assessing the level of structural deterioration at desired inspection frequency. Visual inspection gives superficial surface information about the health of a structure due to the fact that many damages can occur from inside the structure. Understanding the need for a reliable method of assessing the condition of our nation's infrastructure, researchers have been testing the feasibility of many different forms of nondestructive evaluation (NDE) techniques.

Structural health monitoring (SHM) employs NDE techniques to monitor the degradation of a structure over a period of time and helps engineers to determine the optimal time to make necessary and economic repairs before it is too late. The benefit of NDE techniques is that they have the ability to perform subsurface condition assessment without compromising the integrity of the structure. One of the most comprehensive methods of subsurface inspection of reinforce concrete (RC) structures is the electromagnetic (EM) techniques. Both ground penetrating radar (GPR) (often used in contact with the inspected surface) and far-field airborne radar have been investigated for use in subsurface inspection with promising results.[2] GPR has proven useful in the fields of geophysical and geotechnical studies because it is more economically feasible than traditional drilling methods allowing for more frequent and thorough testing.[3] When applied to bridge inspection, GPR proves to be an

Further author information: (Send correspondence to T. Yu)
E-mail: Tzuyang_Yu@uml.edu, Telephone: 1 978 934 2288

Nondestructive Characterization and Monitoring of Advanced Materials, Aerospace, and Civil Infrastructure 2017, edited by H. Felix Wu, Andrew L. Gyekenyesi, Peter J. Shull, Tzu-Yang Yu, Proc. of SPIE Vol. 10169, 101691F · © 2017 SPIE · CCC code: 0277-786X/17/$18 · doi: 10.1117/12.2258658

Downloaded From: https://www.spiedigitallibrary.org/conference-proceedings-of-spie on 8/8/2018
Terms of Use: https://www.spiedigitallibrary.org/terms-of-use

inconvenience because the contact inspection scheme of GPR requires lane closure. In otherwords, traffic needs to be rerouted in order to make measurements. The least disruptive method of bridge inspection should be by remotely assessing structural condition, in a way which measurements can be taken even during rush-hour traffic.

Radar systems operate by transmitting EM signals in the radio frequency band and collecting reflected EM signals containing information about subsurface damage.[4] Applications of radar inspection include material characterization, anomaly detection, rebar detection, corrosion assessment, debonding detection and remote sensing.[4] In these applications a trade off must be made, in order to achieve high resolution images a higher operating frequency must be used, which will result in lower surface penetration.[4] This has been one of the major obsticles of applying this technology to damage detection out in the field. For the purpose of inspection high resolution images and surface penetration are essential to making an accurate assessment about the health of a structure. To address this issue wideband subsurface imaging radar using synthetic aperture radar (SAR) has been developed for the purpose of remote inspection. SAR works differently from other forms of radar inspection because it has the ability to remotely collect subsurface electromagnetic data for spatial analysis with flexible resolution capabilities.

The purpose of this paper is to investigate the use of SAR imaging in corossion detection of steel rebar in free space. First we study how a corroded steel rebar in free space appears in SAR images. A series of experiments were performed using artificially corroded (No. 3 and No. 4) rebar and a continuous wave imaging radar (CWIR) to determine the levels of corrosion that have occured. The experimental methods used will be discussed. Finally the results and data will be analyzed and a summary of the results will be presented along with a conclusion.

2. SYNTHETIC APERTURE RADAR IMAGING

2.1 Background

Synthetic aperture radar (SAR) was developed in the 1950s after Carl Wiley of the Goodyear Aircraft Corporation discovered that a one-to-one relationship exists between a reflected object being linearly traversed by a radar beam and the doppler shift of the signal reflected to the radar by that object.[5] Since this developement the remote sensing abilities of SAR were refined to create high resolution time domain images using a smaller radar antenna. The CWIR used in these experiments is able to send out a wide bandwidth signal for greater range resolution while using a minimal power output.

2.2 Signal Processing

Theoretical basis of SAR imaging and the backprojection algorithm is provided in this section. Fig. 1 is a representation of SAR measurements taken on the image plane where different incident angles (θ_m) and frequencies (ω_n) form a data plot using inverse SAR mode as an example.[6]

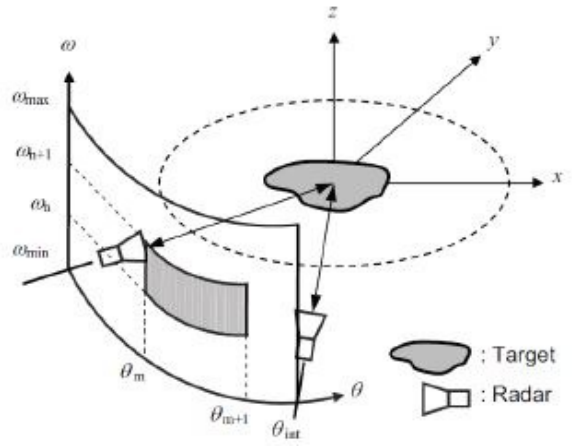

Figure 1. Definition of inspection angle on image plane.[4]

Downloaded From: https://www.spiedigitallibrary.org/conference-proceedings-of-spie on 8/8/2018
Terms of Use: https://www.spiedigitallibrary.org/terms-of-use

A description of the primary steps in SAR imaging are as follows. Collection of SAR point response by the radar system is defined as

$$S(x, ysin\theta_i) = \text{sinc}\left(\frac{\pi sin\theta_i}{\rho_r}\right)\text{sinc}\left(\frac{\pi x}{\rho_{xr}}\right) \tag{1}$$

where (x, y, z) = the coordinate axis on the inspection plane, θ_i = the incident angle with respect to the z axis, the range resolution of the radar is denoted by ρ_r (distance from the radar to the scatterer) and ρ_{rx} = the cross-range resolution of the radar (distance of the path of the radar).[4] The sinc function is represented by $\text{sinc}(x)=\frac{\sin(x)}{x}$. The scattering response $S(\overline{r}_{s,j},t)$ of a single point scatterer represented by the position vector of the J^{th} scatterer $\overline{r}_j$ and is measured by the radar with position vector $\overline{r}_s$ can be expressed as a function of time t and $\overline{r}_{s,j}$:

$$S(\overline{r}_{s,j},t) = \frac{1}{r_{s,j}^2}\int_{\omega_c-\pi B}^{\omega_c-\pi B} d\omega \cdot \exp[i\omega t] \tag{2}$$

Where B = the frequency bandwidth, $\overline{r}_{s,j}$= the difference between $\overline{r}_s - \overline{r}_j$ and $|\overline{r}_{s,j}| = r_{s,j}$, ω_c = the central angular frequency, i = the imaginary number and ω = the independent angular frequency variable. By shifting from t to $\hat{t} = t - \frac{r_{s,j}}{c}$, where c = the speed of the radar signal, range comression on $S(\overline{r}_{s,j},t)$ can be conducted. The integral in Eq.(3) thus becomes:

$$S(\overline{r}_{s,j},\hat{t}) = \frac{B}{r_{s,j}^2}\exp[i\omega_c\hat{t}] \cdot \text{sinc}\big(B\hat{t}\big) \tag{3}$$

After range-compression on all focused radar signals is complete, $D(\varepsilon,\hat{t})$ may be obtained by integrating all range-compressed focused radar signals, where ε = the radars position while traveling along the synthetic aperture. The following equation is a representation of backprojection processing:

$$B_{BP} = C_{BP} \cdot \frac{\partial D(\varepsilon,\hat{t})}{\partial t} \tag{4}$$

where C_{BP} = the backprojection coefficient defined in order to yield an ideal bandpass transfer function. The backprojected SAR image I is finally obtained by

$$I(\overline{r},\phi) = \int_0^{R_s\theta_{int}} d\varepsilon \cdot B_{BP}(\varepsilon,\hat{t}) \tag{5}$$

where$(\overline{r},\phi)$ = polar coordinates on the SAR image range cross-range plane and θ_{int} = the synthetic aperture.

3. EXPERIMENTAL PROCEDURE

3.1 Intact Accelerated Corrosion Test

To characterize the effect of corrosion on steel rebar specimens using SAR images, the corrosion product must remain intact on the surface of steel rebar specimens. The purpose is to correlate SAR images with the corrosion level of steel rebar specimen (quantified by the amount of corrosion or the mass loss measured after the images are obtained). A series of four No. 3 and four No. 4 steel rebars were cut to a length of 250 mm and then measured to determine their initial mass. Each specimen was then placed suspended in a plastic container. A mist of 5% (by mass) NaCl solution was then sprayed onto the specimens at an interval of 24 hours. At each 24-hour interval the specimen was rotated 180 degrees to ensure uniform corrosion on both sides. The No. 3 and No. 4 rebar specimens were paired together and each pair was corroded for different lengths of time (t); $t = 0$ week, $t = 1$ week, $t = 2$ weeks and $t = 4$ weeks. As shown in Fig. 2 and Fig. 3 the different orientations for No. 3 and No. 4 rebar corroded at $t = 0$ week and $t = 2$ weeks, with the top of the rebar on the right side of the image. Orientation was defined as the side of the rebar that faces the radar and was positioned normal to the

Downloaded From: https://www.spiedigitallibrary.org/conference-proceedings-of-spie on 8/8/2018
Terms of Use: https://www.spiedigitallibrary.org/terms-of-use

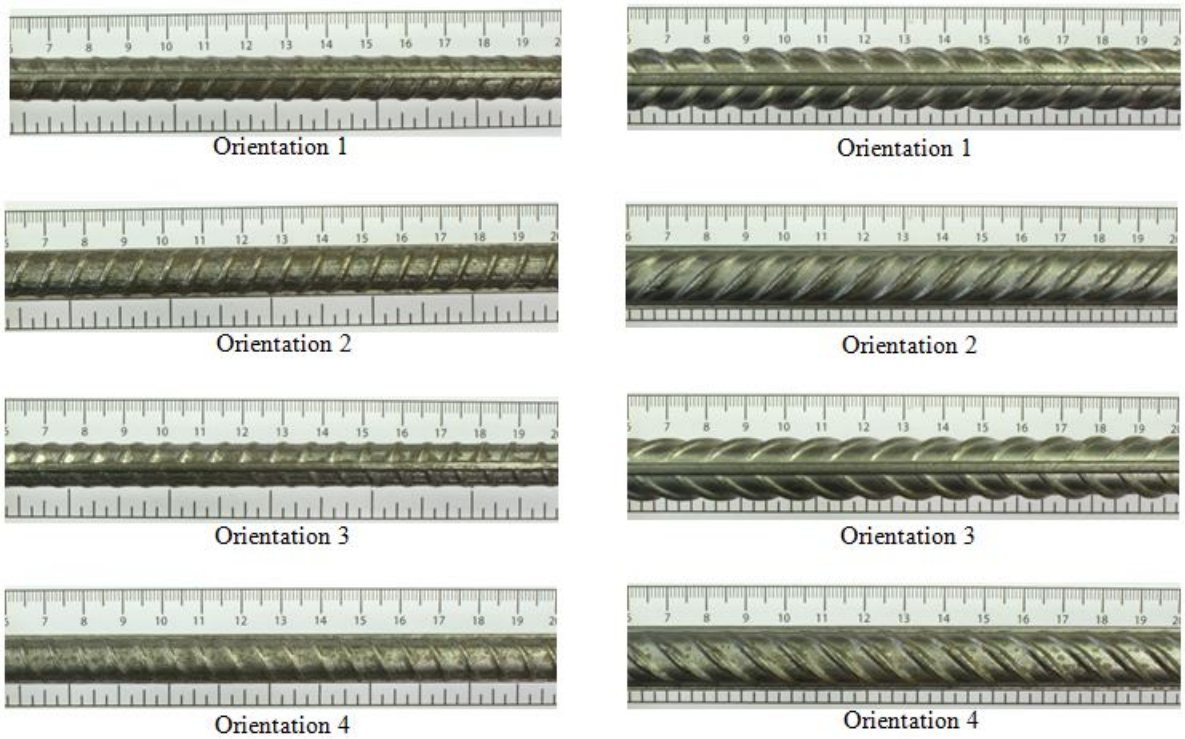

Figure 2. Intact rebar specimens at four orientations ($t = 0$ week)

direction of the outgoing radar signal. When the rebar was arranged vertically each orientation (ort. 1, ort. 2, ort. 3, ort. 4) was 90° from the previous one in a clockwise directions. After each specimen was corroded for the desired length of time, it was stored in a chamber with controlled humidity to prevent any further corrosion from taking place.

3.2 SAR Image Collection

All the radar images were taken inside an anechoic chamber. After some experimentation it was decided the optimal range distance to be 30.4 cm, eliminating the top and bottom signal of each specimen from the radar image, which could cause some interference in the SAR images. The cross range distance also remained constant at 80 cm. The specimens were positioned vertically with respect to the radar by measuring at various levels along the rebar specimens, as shown in Fig. 4. Each rebar specimen was positioned at the midpoint of cross range. The specimen was scanned at a cross range interval of 0.3125 cm, which results in 256 scans in an 80 cm cross range. Each specimen was scanned at all four different orientations in order to make sure all the corrosion was being represented in the scan data. After all the images were collected and processed from each of the specimens. The rebars were then cleaned and a final mass measurement was taken.

4. RESULTS AND ANALYSIS

4.1 SAR Images

The SAR images from all four orientations were averaged for each of the specimens. As shown in Fig. 5, SAR images for the No. 3 rebar at $t = 0$ week and the No. 3 rebar at $t = 4$ weeks were plotted in the range vs. cross-range domain. The color scale was used to indicate the SAR amplitude at a given point within the image. The SAR amplitude distribution in the $t = 0$ week was different from the $t = 4$ weeks. It was found that, as corrosion time increases, the amount of corrosion accumulating on the specimens increases lowering the specular return of the rebar specimen. This amplitude reduction was caused by the formation of surface rust (lower dielectric constant than steel) and the scattering effect of rust geometry (rough surface of the surfaces rust).

Downloaded From: https://www.spiedigitallibrary.org/conference-proceedings-of-spie on 8/8/2018
Terms of Use: https://www.spiedigitallibrary.org/terms-of-use

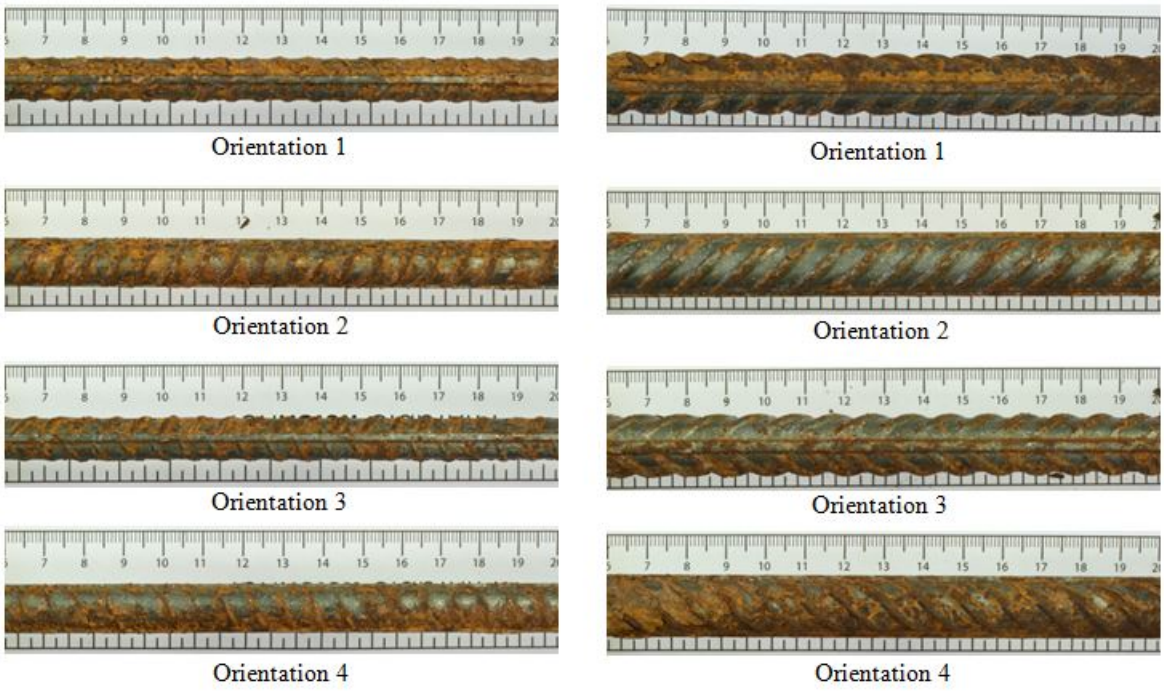

Figure 3. Corroded rebar specimens at four orientations ($t = 2$ weeks)

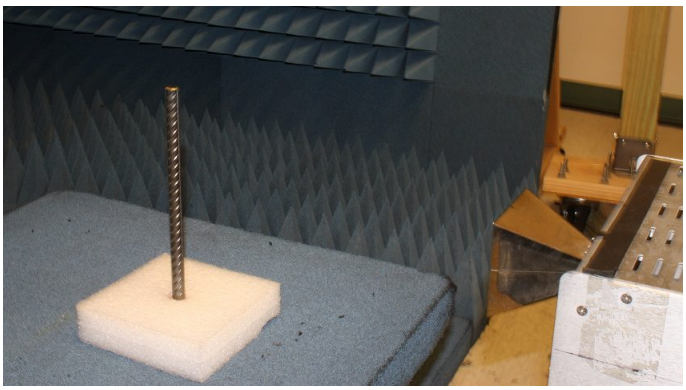

Figure 4. Experimental configuration of SAR imaging inside an anechoic chamber

To get a better idea of the difference in maximum amplitudes between the two specimens it is necessary to look at the plots of amplitude vs. range and amplitude vs. cross-range at the point of maximum amplitude (I_{max}). Fig. 6 clearly shows the difference in amplitudes between the $t = 0$ week rebar and the $t = 4$ weeks rebar. The presence of corrosion causes a reduction in I_{max} because of the lower dielectric constant that corrosion product has compared to bare steel. The measurement of I_{max} does not, however, take into consideration the level of corrosion on the entire rebar but rather focuses on a specific point in the range vs. cross-range domain.

4.2 Integrated SAR amplitude

A better representation of the level of corrosion on the entire rebar is to calculate a single value by integration of the plot in Fig. 5. Shown in Fig. 7 is a plot of the integrated SAR amplitude (I_{SAR}) with respect to time of corrosion for No. 3 and No. 4 rebar. For the No. 3 rebar at $t = 0$ week I_{SAR} is remarkably less than that of the No. 4 rebar at $t = 0$ week. This is due to the difference in surface area of the rebar, because the No. 4 rebar has

Downloaded From: https://www.spiedigitallibrary.org/conference-proceedings-of-spie on 8/8/2018
Terms of Use: https://www.spiedigitallibrary.org/terms-of-use

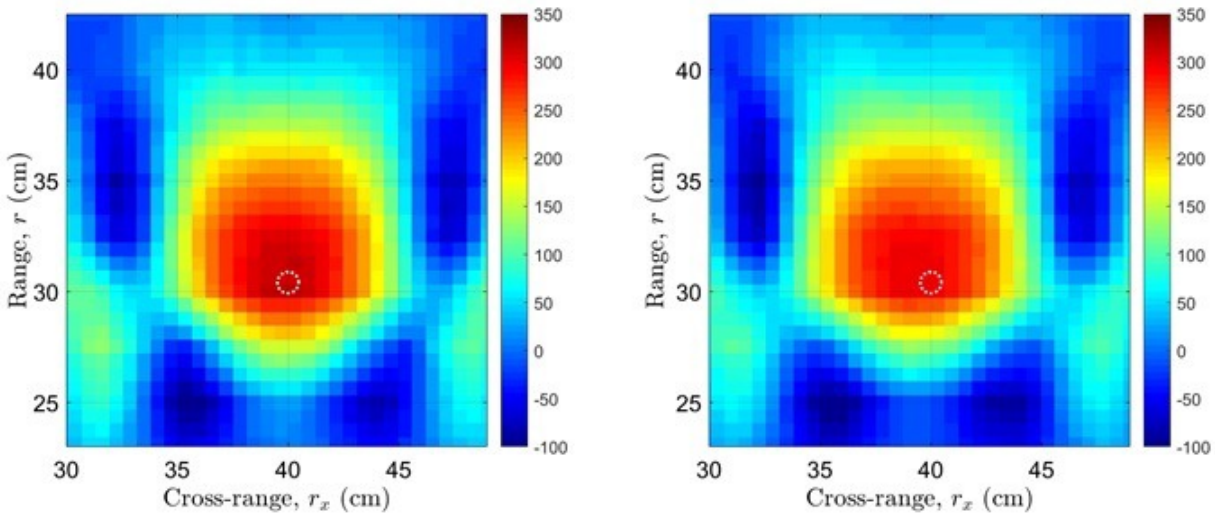

Figure 5. SAR images of No. 3 rebar $t = 0$ week left, $t = 4$ weeks right

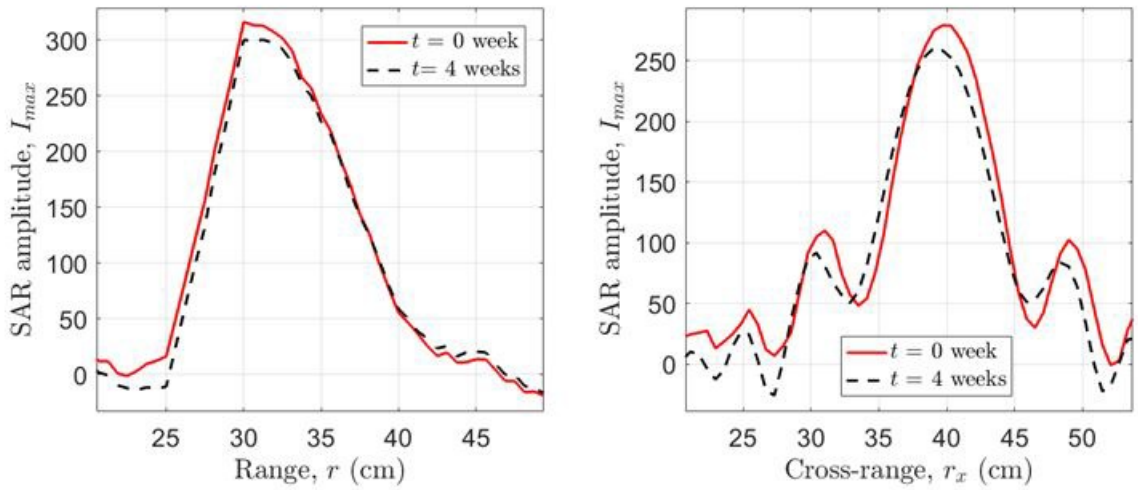

Figure 6. Amplitude vs. range and amplitude vs cross-range at maximum amplitude for $t = 0$ week, $t = 4$ weeks

Downloaded From: https://www.spiedigitallibrary.org/conference-proceedings-of-spie on 8/8/2018
Terms of Use: https://www.spiedigitallibrary.org/terms-of-use

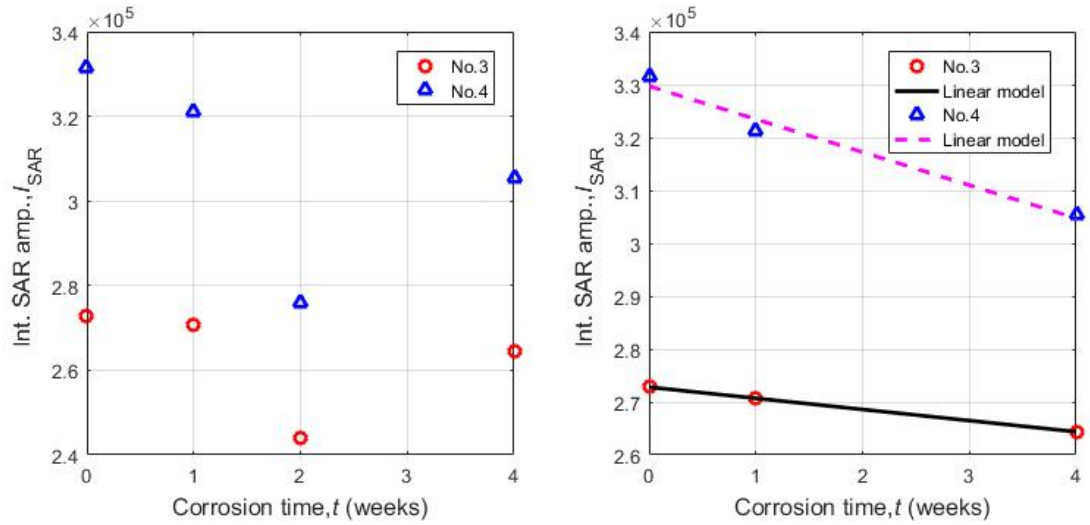

Figure 7. Integrated SAR amplitude vs. corrosion time; (left) experimental measurements, (right) proposed linear models

Table 1. Model parameters

	C_1	C_2	R^2
No. 3	-2107.7	2.726×10^5	.9998
No. 4	-6242.35	3.297×10^5	.9760

a larger surface area it naturally has a larger I_{SAR}. The effect corrosion time has on I_{SAR} is modeled in Eq. (6).

$$I_{SAR}(t) = C_1 t + C_2 \tag{6}$$

where $I_{SAR}(t)$ = the integrated SAR amplitude, C_1 and C_2 = constants, and t = corrosion time ($weeks$). In this linear model the No. 4 rebar has a larger negative slope than the No. 3 rebar. This is because as corrosion time increases the amount of corrosion accumulating on a No. 4 rebar is greater than on a No. 3 rebar due to it having a larger surface area. The $t = 2$ week corrosion sample for both the No. 3 and No. 4 rebar are considered outliers and do not follow this trend and have been left out of the linear model. This may be explained by different corrosion conditions or perhaps by a different material make up of the specimen. Another explanation may be that the geometry of the specimen may cause an unusual scattering pattern leading to a lower I_{SAR}. Fig. 8 takes a closer look at the comparison of I_{SAR} for the two different rebar sizes at: $t = 0$ week, $t = 1$ week $t = 2$ weeks, and $t = 4$ weeks.

4.3 Mass loss and Corrosion Rate Modeling

To quantify the amount of corrosion that has accumulated on a specimen it must be expressed it in terms of mass loss (ΔM). The plot in Fig. 9 shows the effect increasing time has on ΔM for both the No. 3 rebar and No. 4 rebar, this effect is modeled by Eqs. (7) and (8).

$$\Delta M(t) = C_3[\exp(C_4 t) - 1] \tag{7}$$

$$\frac{d\Delta M(t)}{dt} = C_3 C_4 \exp[C_4 t] \tag{8}$$

Downloaded From: https://www.spiedigitallibrary.org/conference-proceedings-of-spie on 8/8/2018
Terms of Use: https://www.spiedigitallibrary.org/terms-of-use

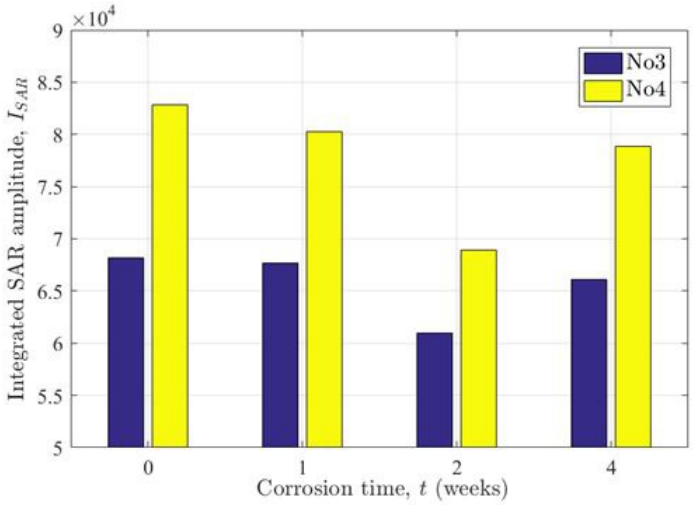

Figure 8. Integrated SAR amplitude vs. corrosion time

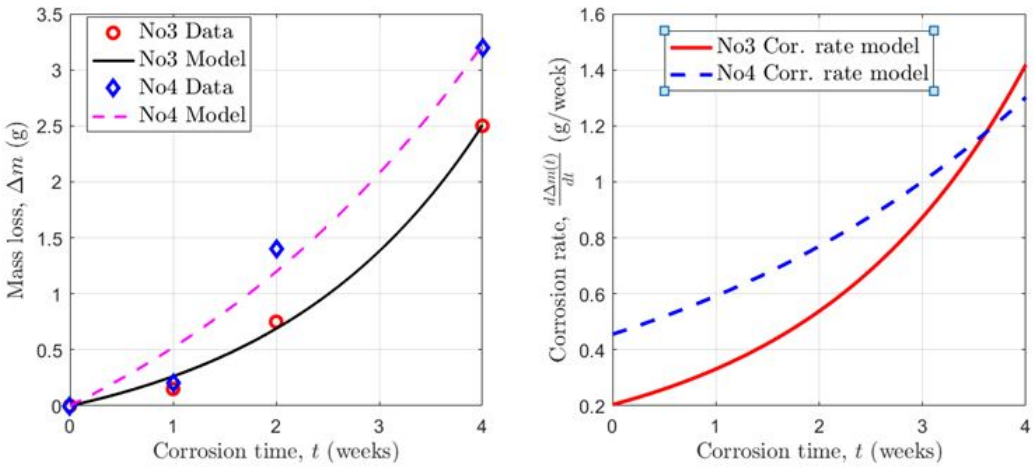

Figure 9. Mass loss vs. corrosion time

where $\Delta M(t)$ = the mass loss (g), C_3 and C_4 = constants, t =corrosion time $(weeks)$, $\frac{d\Delta M(t)}{dt}$ = the rate of corrosion $(\frac{g}{week})$ and R^2 = the coefficient of determination. As expected an increase of corrosion time leads to increasing ΔM. It is also obvious from looking at the corrosion rate vs. corrosion time graph that the No. 4 rebar at least for the first 3.5 weeks has a high rate of corrosion than the no. 3. This supports the findings from Fig. 7 because I_{SAR} decreases at a higher rate for the No. 4 rebar.

Table 2. Model parameters

	C_3	C_4	R^2
No. 3	.4208	.4848	..9958
No. 4	1.734	.2626	.9777

Downloaded From: https://www.spiedigitallibrary.org/conference-proceedings-of-spie on 8/8/2018
Terms of Use: https://www.spiedigitallibrary.org/terms-of-use

5. CONCLUSION

In this paper, the use of SAR imaging for corrosion detection of steel rebar in free space was explored. It was found that the presence of corrosion (because it has a lower dielectric constant than bare steel and a rough surface geometry) has an effect on the SAR amplitude distribution and decreases the maximum SAR amplitude. The integrated SAR amplitude was also found to decrease with increasing corrosion time, with the No. 4 rebar decreasing at a greater rate than the No. 3 rebar. The rate of mass loss with respect to time was found to be greater for the No. 4 rebar than the No. 3 rebar, as expected. From our positive results, the use of SAR imaging for corrosion detection is demonstrated. It is believed that SAR imaging can be applied for practical corrosion detection in the future.

REFERENCES

1. A. W. Herrmann, "Asce 2013 report card for america's infrastructure," in *IABSE Symposium Report*, **99**(33), pp. 9–10, International Association for Bridge and Structural Engineering, 2013.
2. T.-Y. Yu and O. Büyüköztürk, "A far-field airborne radar ndt technique for detecting debonding in gfrp–retrofitted concrete structures," *NDT & E International* **41**(1), pp. 10–24, 2008.
3. K. F. Lee, "A case study of ground penetrating radar for non-destructive testing applied to underground culvert structures," *Journal of Emerging Trends in Engineering and Applied Sciences* **2**(6), pp. 1079–1082, 2011.
4. T. Yu, C.-F. Su, C.-P. Lai, and H. F. Wu, "Wideband subsurface radar for bridge structural health monitoring and nondestructive evaluation," in *SPIE Smart Structures and Materials+ Nondestructive Evaluation and Health Monitoring*, pp. 86940I–86940I, International Society for Optics and Photonics, 2013.
5. C. R. Jackson, J. R. Apel, *et al.*, *Synthetic aperture radar: marine user's manual*, US Department of Commerce, National Oceanic and Atmospheric Administration, National Environmental Satellite, Data, and Information Serve, Office of Research and Applications, 2004.
6. V. Le, T. Yu, J. O. Twumasi, and Q. Tang, "Sizing and ranging criteria for sar images of steel and wood specimens," in *SPIE Smart Structures and Materials+ Nondestructive Evaluation and Health Monitoring*, pp. 980404–980404, International Society for Optics and Photonics, 2016.

Downloaded From: https://www.spiedigitallibrary.org/conference-proceedings-of-spie on 8/8/2018
Terms of Use: https://www.spiedigitallibrary.org/terms-of-use